

Various electronic crystal phases in rhombohedral graphene multilayers

Wangqian Miao^{1, 2, *} and Chu Li³

¹Department of Physics, The Pennsylvania State University, University Park, Pennsylvania 16802, USA

²Department of Physics, The Hong Kong University of Science and Technology, Clear Water Bay, Hong Kong, China

³Department of Chemistry, Northwestern University, Evanston, IL 60208, USA

(Dated: December 30, 2025)

We systematically investigate the emergence of electronic crystal phases in rhombohedral multilayer graphene using comprehensive self-consistent Hartree Fock calculations combined with *ab initio* tight binding model. As the carrier density increases, we uncover an isospin cascade sequence of phase transitions that gives rise to a rich variety of ordered states, including electronic crystal phases with non-zero Chern numbers. We further show the nearly degeneracy of these topological electronic crystals hosting extended quantum anomalous Hall effect (EQAH) in the mean field regime and characterize pressure driven phase transitions. Finally, we discuss the thermodynamic signatures, particularly the behavior of the inverse compressibility, in light of recent experimental observations.

I. INTRODUCTION

In the dilute limit of a two dimensional electron gas, kinetic energy is quenched by Coulomb interactions and the electrons spontaneously crystallize into a Wigner crystal. This phenomenon becomes even more intriguing when the underlying electronic bands carry non trivial topology, which may carry integer Chern number [1–6].

Experiments on rhombohedral multilayer graphene [7–9] (RMG) have revealed a quantized Hall effect and even fractional Hall signals upon slight electron doping. The most striking observation is an extended quantum anomalous Hall (QAH) phase that persists in the regime where a strong displacement field pushes the electrons away from the aligned hBN substrate. This suggests that moiré effects are relatively weak in this setup, especially when compared with systems such as twisted MoTe₂. Recent nano-ARPES studies [10, 11] indicate that hBN alignment enhances band flatness, in qualitative agreement with quantum capacitance data showing that stronger incompressibility emerges mainly at integer filling factors at moiré proximal region [12]. These findings naturally raise the question of the microscopic mechanism behind the insulating phase: is it predominantly driven by electron–electron interactions [13–29], or does it still originate from residual hBN alignment [30]? From a theoretical perspective, the single-particle Hamiltonian of RMG is relatively simple to investigate: its low-energy physics can be captured by a *n*-th order Dirac Hamiltonian [31] acting in the layer degree of freedom, effectively describing the first conduction and first valence bands. Remarkably, these bands resemble drumhead surface states [32] in the bulk limit, which helps to explain both their pronounced flatness in the conduction band bottom and their close analogy to the zeroth Landau level [23, 33].

In this work, we employ an *ab initio* tight binding

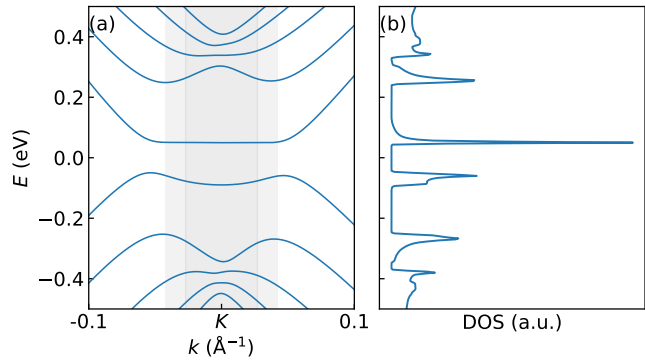


FIG. 1. Single particle band structure (a) of rhombohedral penta layer graphene (R5G) near the K point for a displacement field of $U = 0.035$ eV, and the corresponding density of states (b). The van Hove singularity in the first conduction band originates from the flat band bottom. The shaded area labels the region when the electron filling is $0.5 \times 10^{12} \text{ cm}^{-2}$ and $1.2 \times 10^{12} \text{ cm}^{-2}$, respectively.

model [34] for rhombohedral multilayer graphene and systematically map out the Hartree Fock phase diagram as a function of carrier density n and displacement field. Within our mean field framework, we allow for spontaneous breaking of translational symmetry, as well as spin SU(2) and valley U(1) symmetries, to capture the onset of electron crystallization. A central outcome is a cascade of isospin phase transitions driven by a Stoner instability [35], closely analogous to that inferred from inverse-compressibility measurements in rhombohedral trilayer graphene [36]. In the same parameter regime, we identify a sequence of electronic crystal phases, both topologically trivial and with nonzero Chern number, that energetically outperform the corresponding Fermi-liquid (FL) states at the mean-field level and emerge as stripe-like regions in the phase diagram. Notably, anomalous Hall crystal phases can exist even at relatively high doping, around $n \approx 3 \times 10^{12} \text{ cm}^{-2}$, at appropriate displacement fields. Motivated by experiments, we then focus on

* Contact author: wqmiao@psu.edu

the density range near $n \approx 1 \times 10^{12} \text{ cm}^{-2}$. In this regime, our numerics reveal strong competition among multiple electronic phases with nearly degenerate energies, suggesting that phase coexistence or mesoscale inhomogeneity may be relevant. This sensitivity also underscores the key role of hBN alignment in stabilizing the QAH state in experiment. Finally, we discuss how moderate hydrostatic pressure can readily tune the WC–AHC transition while largely preserving the favorable quantum geometry of the bands. We conclude by discussing the thermodynamic signatures of these phase transitions, with particular emphasis on the behavior of the inverse compressibility.

II. MICROSCOPIC HAMILTONIAN

A. Slater–Koster tight binding model for Rhombohedral multilayer Graphene

To describe the low-energy electronic structure of rhombohedral multilayer graphene (RMG), we employ a Slater–Koster (SK) parameterization of the p_z -orbital tight-binding Hamiltonian recently developed in Ref. [34], benchmarked against density functional theory (DFT). The hopping amplitude between two p_z orbitals separated by vector \mathbf{r} with vertical projection $z = \hat{z} \cdot \mathbf{r}$ is written as

$$t_{\text{SK}}(r) = V_{pp\pi} \left(1 - \frac{z^2}{r^2}\right) e^{q_\pi(1-r/a_\pi)} f_c(r) + V_{pp\sigma} \frac{z^2}{r^2} e^{q_\sigma(1-r/a_\sigma)} f_c(r), \quad (1)$$

where $f_c(r) = (1 + e^{(r-r_c)/l_c})^{-1}$ is a smooth cutoff function in the real space. The optimized parameters fitted from density functional theory are $V_{pp\pi} = -2.81 \text{ eV}$, $V_{pp\sigma} = 0.48 \text{ eV}$, $a_\pi = 1.418 \text{ \AA}$, $a_\sigma = 3.349 \text{ \AA}$, $q_\pi = 3.145$, $q_\sigma = 7.428$, $r_c = 6.14 \text{ \AA}$, $l_c = 0.265 \text{ \AA}$. Beyond nearest-layer couplings, we include a small second-neighbor interlayer hopping $t_2 \approx -7 \text{ meV}$, which is essential for reproducing the small intrinsic gap of trilayers.

Two additional single-particle terms account for experimentally relevant symmetry-breaking effects. An inversion-symmetric potential (ISP) distinguishes outer and inner layers,

$$[H_{\text{ISP}}]_{ll'} = V_{\text{ISP}} \delta_{ll'} \left| l - \frac{n+1}{2} \right|, \quad (2)$$

with $V_{\text{ISP}}/d_0 \approx 5 \text{ meV/\AA}$, where $d_0 \approx 3.33 \text{ \AA}$ is the interlayer spacing of adjacent carbon layers. A perpendicular displacement field is modeled as a linear layer-dependent potential,

$$[H_D]_{l\alpha,l'\beta} = U \left(l - \frac{n-1}{2} \right) \delta_{ll'} \delta_{\alpha\beta}, \quad (3)$$

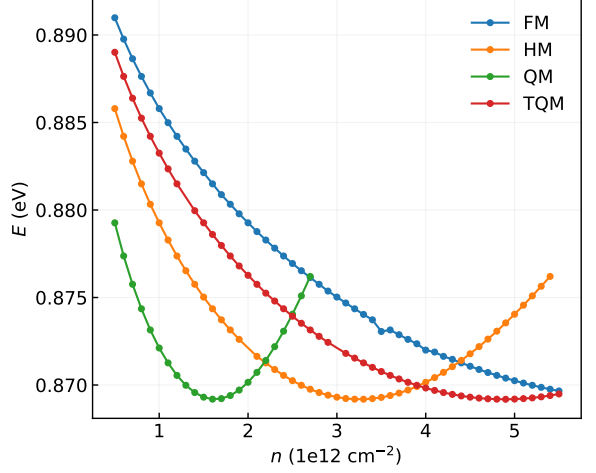


FIG. 2. Cascade of isospin phase transitions in R5G. QM denotes the quarter metal phase, HM the half metal phase, TQM the three quarter metal phase, and FM the full metal phase. The Hartree Fock results indicate a first order phase transition as the carrier density n increases.

with $U \propto -|e|d_0 D$. Together, these terms capture the tunable interlayer asymmetry and gap opening under external fields. This SK Hamiltonian provides a microscopic foundation for our continuum modeling and phase diagram analysis of RMG.

When the displacement field induced onsite potential satisfies $u > 0$, the conduction band electrons become predominantly localized on the B_N orbital, while the valence-band electrons localize mainly on the A_1 orbital. This naturally leads to an effective two-band description within the A_1 – B_N subspace. For $u < 0$, the situation is reversed. It is worth noting that, in the bulk limit and in the absence of a displacement field, rhombohedral multilayer graphene is a nodal-line semimetal whose geometric configuration closely resembles a three dimensional SSH model. The lowest energy surface bands in this limit correspond to the characteristic drumhead states associated with the nodal line topology [32, 33]. A representative single particle band structure near the atomic K valley is shown in Fig. 1(a) for $u = 0.035 \text{ eV}$. In this case, the conduction-band minimum is remarkably flat, and the associated van Hove singularity lies in the same energy window. Note that these bands are nearly fourfold degenerate due to the spin and valley degrees of freedom. Consequently, one may anticipate a Stoner-type instability once the criterion $\rho(E)U > 1$ is satisfied, where $\rho(E)$ is the density of states at the Fermi level E and U is the effective Hubbard interaction [36].

B. Mean field treatment

To capture the Coulomb interaction in the low doping regime, we retain its long range component and neglect

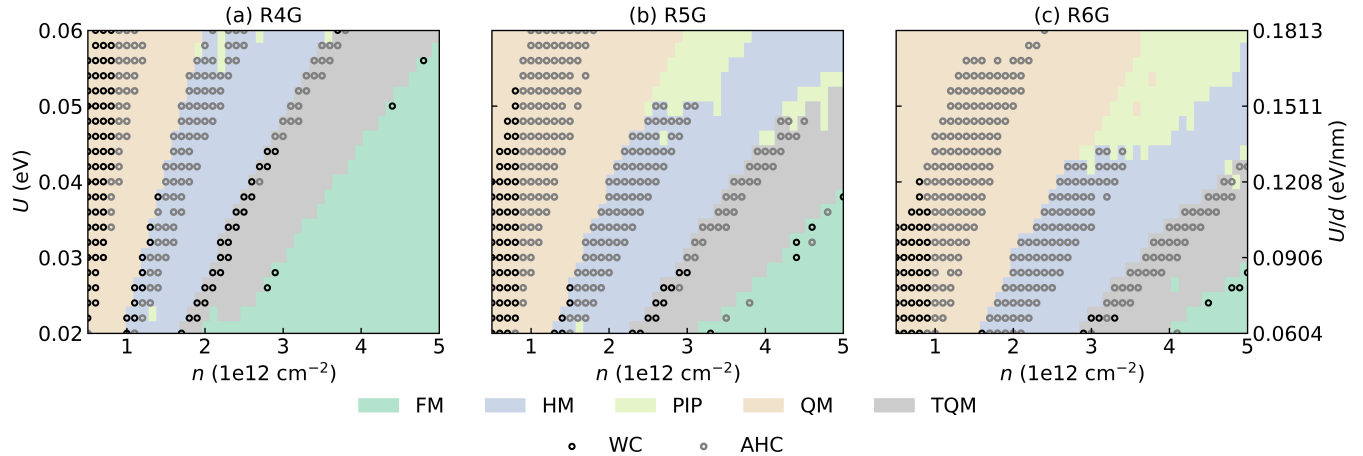


FIG. 3. Hartree–Fock mean-field phase diagrams of rhombohedral graphene multilayers as functions of electron doping density n and displacement field U : (a) tetralayer (R4G), (b) pentalayer (R5G), and (c) hexalayer (R6G). QM, HM, TQM, and FM denote the quarter-metal, half-metal, three-quarter-metal, and full-metal phases, respectively. PIP indicates a partially isospin-polarized state. Across the isospin-driven phase transitions, symmetry-broken electronic crystal phases—Wigner crystal (WC) and anomalous Hall crystal (AHC)—can also emerge. The annotated regions additionally label the number of isolated flat bands participating at the Fermi level: 1 in QM, 2 in HM, 3 in TQM, and 4 in FM.

the short range part [28, 37–39] to perform self-consistent Hartree Fock calculations. The interacting part is written as,

$$H_{\text{int}} = \frac{1}{2} \sum_{\mathbf{q}} v(\mathbf{q}) : \rho_{\mathbf{q}} \rho_{-\mathbf{q}} :, \quad (4)$$

The density operator written in the plane wave basis is

$$\rho_{\mathbf{q}} = \sum_{\mathbf{k}} \sum_{s\mu\alpha} c_{\mathbf{k}+\mathbf{q},s\mu\alpha}^{\dagger} c_{\mathbf{k},s\mu\alpha}. \quad (5)$$

where s is the spin index, μ is the valley index and α is the joint index for sublattice (σ) and layer (l). The screened interaction is taken as [29],

$$v_{ll'}(\mathbf{q}) = \frac{e^2}{2S \epsilon_r \epsilon_0 q} \times \begin{cases} \tanh(qd_s), & l = l', \\ e^{-q|l-l'|d_0}, & l \neq l'. \end{cases} \quad (6)$$

where $d_s = 10$ nm is the gate distance, d_0 is the interlayer distance of graphene layers, S is the total area and $\epsilon_r = 5$ is the dielectric constant. For a fixed carrier density n , the real-space lattice constant (and hence the superlattice length scale) is uniquely determined:

$L_s = \sqrt{2/\sqrt{3}n}$ for the hexagonal lattice and $L_s = \sqrt{1/n}$, for the square lattice. We initialize the single particle density matrix by randomly distributing electrons among the spin valley sectors and iteratively solve the Hartree Fock Dyson equation to self-consistency. The zero-temperature ground state is then identified as the converged solution with the lowest condensation energy among competing phases. Further computational details are provided in Appendix B, and two recent reviews of Hartree Fock formalism for moiré materials are also presented in Ref. [40, 41].

III. ELECTRONIC CRYSTAL PHASES

A. Isospin phase transition and full phase diagram

When the first conduction band of rhombohedral multilayer graphene (RMG) is electron doped toward the van Hove singularity (VHS), a Stoner instability is expected to occur, potentially generating a cascade of isospin phase transitions [35, 42–44]. Such a cascade has already been explored experimentally in rhombohedral trilayer graphene (R3G) [36]. In our HF calculations, the isospin transitions in RMG appear as first order transitions at the mean field level, as depicted in Fig. 2.

A natural question is whether, near these isospin transitions, translational-symmetry-breaking electronic crystal phases can simultaneously emerge and even become energetically favorable compared with the corresponding isospin polarized Fermi liquids. To address this, we map out the phase diagram of RMG, including the isospin transitions, and highlight the parameter regions where electronic crystal phases are the mean-field ground states (Fig. 3). The geometry for these electronic phases is fixed as hexagonal. We find that multiple states with distinct occupations among the four spin valley sectors (K, \uparrow) , (K, \downarrow) , (K', \uparrow) , and (K', \downarrow) appear when the electron density is around $n \approx 3 \times 10^{12} \text{ cm}^{-2}$. A prominent and robust feature is that electronic crystal phases occur preferentially in the vicinity of the isospin phase transitions, for our tetralayer, pentalayer, and hexalayer results. We also find the trend that the electronic state can appear at the higher doping density region when increasing the number of layers. Related electronic crystal phases emerging in the half-metal regime have also been discussed recently [45, 46]. Finally, when only the long-

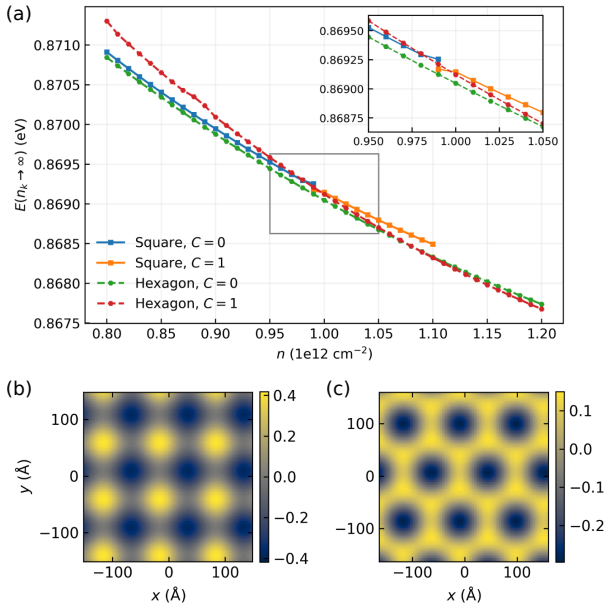


FIG. 4. Competition among different electronic crystal phases in R5G as the electron density n varies, with the displacement field fixed at $U = 0.035$ eV. (a) The energy differences between the square-lattice states ($C = 0/1$) and the hexagonal-lattice states ($C = 0/1$) are relatively small. In certain density ranges, the square-lattice phases compete closely with the hexagonal ones. Density profile $(\rho(r) - \langle \rho(r) \rangle) \Omega_0$ when $n = 1 \times 10^{12} \text{ cm}^{-2}$ for (b) hexagonal AHC (c) square AHC. Ω_0 is the superlattice size.

range Coulomb interaction is retained, several competing topological states can be nearly degenerate in this region due to the $SU(2)_- \times SU(2)_+$ symmetry [47]. Additional short range interaction (for example, intervalley Hund's coupling) and intrinsic spin orbital coupling [37–39, 47] can lift this degeneracy and favor either a fully spin polarized state or a spin valley locked state. Furthermore, this can also explain the absence of triple quarter metal (TQM) phases in experiments [36, 48]. We also note that, in the density window $n \approx (4\text{--}5) \times 10^{12} \text{ cm}^{-2}$, these electronic crystal states remain higher in energy than the fully symmetric metallic phase (FM) in our calculations.

B. Competing phases and pressure effects in the spin valley polarized case

For the tetralayer and pentalayer cases, we further find that the spin-valley polarized anomalous Hall crystal (AHC) phases persist over a relatively wide density range at suitable displacement fields. Recent experiments in R5G/hBN reported an extended quantum anomalous Hall (EQAH) regime: a robust $R_{xy} \approx h/e^2$ plateau with strongly suppressed R_{xx} persisting over a wide density window, often accompanied by hysteresis and a pronounced sensitivity to temperature and bias

current [7, 8]. This phenomenology suggests that EQAH is not a single rigid commensurate phase and a deeper understanding for such phenomena is needed.

Our HF results provide a microscopic basis for such a landscape. At fixed $U = 0.035$ eV, Fig. 4 shows that square lattice and hexagonal lattice electronic crystal states—including both Wigner crystal (WC) and anomalous Hall crystal (AHC) candidates—are nearly degenerate in energy over an appreciable density window ($n \sim 10^{12} \text{ cm}^{-2}$). This near degeneracy implies that weak perturbations (strain, pressure, residual substrate-potential, device inhomogeneity, and disorder [49, 50]) can readily select the preferred crystal geometry and topological sector. In this scenario, an extended $C = 1$ plateau can arise because the system can preserve a quantized Hall response while reorganizing among nearly degenerate AHC realizations as n is tuned, rather than being locked to a unique commensurate state [8]. Moreover, small energy splittings near the WC–AHC boundary naturally promote metastability and hysteresis. Upon increasing temperature, the AHC phase may melt into a distinct metallic state at half filling, often discussed in terms of a composite Fermi liquid (CFL), with an enlarged real-space periodicity compared to the AHC, we do not consider such finite temperature phases here, but they have been reported experimentally in the tetralayer and pentalayer systems [8]. Another important distinction between the AHC and the WC is the comparatively reduced stiffness of the AHC [29, 51], which is attributed to the Wannier obstruction [52] of the underlying Chern band. This is directly visible in the density profiles of different AHC states in Fig. 4(b)(c). A reduced stiffness can enhance the susceptibility to depinning and sliding [53, 54] under an in-plane electric field which leads to deviations from integer Hall response in experiment. Furthermore, a current induced many body breakdown of the AHC state at sufficiently large drive may appear [55].

To further investigate this near degeneracy, we introduce pressure as an additional tuning knob. In graphene/hBN moiré structures, pressure is known to substantially modify the band structure and can enhance the effective moiré potential by reducing the interlayer separation [56]. In moiré TMDs, pressure has also been proposed as a route to optimize band geometry [57, 58] to approach an ideal trace condition and thereby influence the competition between charge orders and topological correlated phases. Here, motivated by these developments and by the EQAH phenomenology [8], we examine how pressure reshapes the WC–AHC competition in our model. Importantly, in our calculations pressure is implemented only through the pressure-dependent intrinsic band parameters of R5G and we do not include any pressure-induced change of the moiré potential strength. The interlayer distance and bonding length of carbon atoms is determined through density functional theory, see Appendix A. Then the pressure effect on R5G is reflected through the *ab initio* tight binding model described in Sec. II A. Within this assumption, we first

shown the calculated phase diagram for R5G at 0.5 GPa and 1.0 GPa separately in Fig. 5 (a)-(b). Our results illustrate that the electronic crystal states can be further stabilized at higher doping range when. Fig. 5(c) shows that the electronic crystal phases extended in the phase diagram while the AHC stable region shrinks as pressure increases. Nevertheless, Fig. 5(d) shows near the WC–AHC transition, for moderate pressure $P \lesssim 1.5$ GPa, the trace condition $T \simeq 0.1$ [13] (dark region in Fig. 5-(b)). This value is defined as,

$$T = \frac{1}{2\pi} \int d\mathbf{k} (\text{Tr}(g(\mathbf{k}) - |\Omega(\mathbf{k})|)), \quad (7)$$

where $g_{\mu\nu}(\mathbf{k})$ is the Fubini-Study metric and $\Omega(\mathbf{k})$ is the Berry curvature. This close to zero numeric indicates that the pressure-induced suppression of AHC in our calculation is not primarily driven by a degradation of the ideal band geometry condition. We further note that a patterned gate capable of manually modulating the electrostatic potential on the graphene layers may provide an experimental handle to control the pinning of these electronic crystal states [59–61].

Finally, we emphasize that our analysis is based on static mean field HF energetics and therefore does not include correlation energy beyond HF [20, 62]. HF theory is known to overestimate the tendency toward crystallization in the two-dimensional electron gas [20]. However, recent variational Monte Carlo studies demonstrate that Berry curvature of the parent band can dramatically enhance crystallization [63]. Given the small HF energy differences in Fig. 4, the correlation effects may be decisive near the WC–AHC boundary. Incorporating correlation energy beyond HF, as well as the experimentally relevant pressure-enhanced moiré potential, is therefore an important direction for future work [20, 56, 64].

IV. DISCUSSION

We discover multiple phase transitions numerically within our mean field treatment of RMG, and we now discuss their thermodynamic signatures in connection with recent experiments [12]. The cascade of isospin phase transitions shown in Fig. 2 is closely related to the stripe-like regions of negative inverse compressibility observed near integer fillings in R5G, where the inverse compressibility is defined as $K^{-1}(n) = \partial\mu/\partial n$, with μ the intrinsic chemical potential of the electronic subsystem.

A useful thermodynamic reference point is a first order transition with macroscopic phase coexistence: the Maxwell construction yields a mixed phase window with constant μ and hence $K^{-1} = 0$ in the thermodynamic limit. In contrast, experiments typically show additional “shadow” features in the inverse compressibility, including negative dips, rather than a broad $K^{-1} \approx 0$ plateau. This phenomenology is observed both across the isospin phase transitions and near the metal–insulator boundary. More specifically, Ref. [12] focuses on the moiré

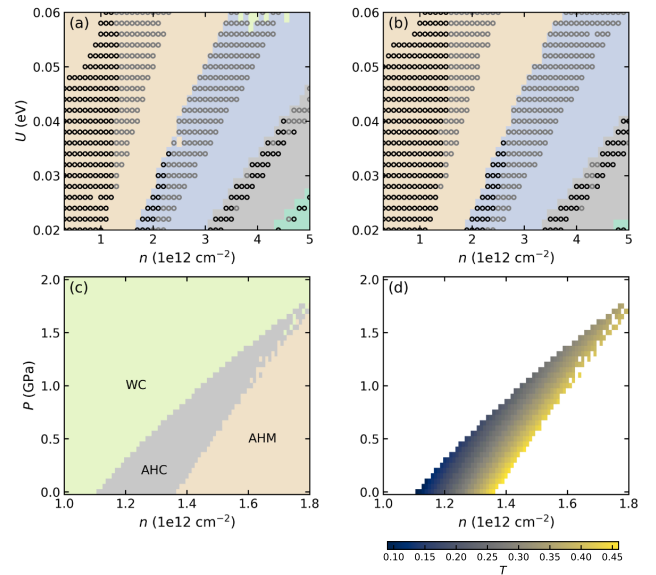


FIG. 5. Pressure induced phase transition in rhombohedral pentalayer graphene (R5G) (a) The same phase diagram as Fig. 3 when $P = 0.5$ GPa (b) when $P = 1.0$ GPa. The same color legend has been adopted here. (c) Hartree Fock phase diagram as a function of pressure P and doping density n at fixed displacement field $U = 0.035$ eV. AHM represents the anomalous Hall metal (AHM) region. (d) Trace condition T corresponding to the anomalous Hall crystal (AHC) phases identified in (c). The dark colored region marks the optimal trace condition, located near the WC–AHC phase transition boundary.

proximal region and reports negative inverse compressibility signatures near the quantum freezing region at fractional fillings ($\nu = 1/2, 2/3$ which corresponds to $n \approx (0.4 - 0.6) \times 10^{12} \text{ cm}^{-2}$), where these incompressible phases are interpreted as topological charge density waves (TCDWs) with Chern number $C = -1$ at small magnetic field. Notably, this regime overlaps with the electronic crystal phases in our calculations.

The sharp negative inverse compressibility [65, 66] features cannot be explained by simple macroscopic two-phase coexistence. Instead, long range Coulomb interactions provide a natural route to such behavior: they strongly penalize macroscopic charge separation and can favor intermediate regimes with mesoscopic domain patterns, sometimes discussed as electronic microemulsions [67]. Moreover, the resulting phase competition and inhomogeneous coexistence can be further shaped by disorder potentials [49, 50].

In realistic gated devices, further care is required because the experimentally inferred compressibility contains both intrinsic and geometric electrostatic contributions. The total thermodynamic potential includes the classical charging energy associated with transferring charge to and from gate electrodes, which can be recast as a geometric capacitance term [68]. Consequently, a negative value of $\partial\mu/\partial n$ for the intrinsic electronic sub-

system does not necessarily imply an instability of the full device, since the geometric contribution can restore the stability of the total response. In our Hartree Fock treatment, we impose global neutrality by removing the $q = 0$ Hartree component, equivalently setting $V(q = 0) = 0$, so that the remaining interaction captures intrinsic electronic thermodynamics. It is instructive to contrast this with dynamic mean field theory (DMFT) calculations of magic angle twisted bilayer graphene in the heavy fermion language [68, 69], where negative inverse compressibility can arise from charge reshuffling between localized and itinerant degrees of freedom upon doping. Once geometric capacitance contributions are included, the negative compressibility regions are often strongly reduced, again emphasizing that negative experimental signals need not correspond to a thermodynamic instability of the full electrostatic environment.

We end this paper by noting that recent reported evidence of chiral superconductivity in R4G, R5G [70], and R6G [71] and bubble-like TCDWs in R6G [71] at electron dopings of roughly $(0.5\text{--}1.0) \times 10^{12} \text{ cm}^{-2}$ overlap with the topological electronic crystal regimes in our mean field

phase diagram, suggesting a complex interplay between superconductivity and competing electronic orders. In these experiments the hBN layers are not aligned with the RMGs.

V. ACKNOWLEDGMENT

W. Miao acknowledges X. Dai and B. Yan for stimulating discussion on this topic and recognizes the Penn State Institute for Computational and Data Sciences (RRID:SCR025154) for providing access to computational research infrastructure within the Roar Core Facility (RRID: SCR026424).

VI. CODE & DATA AVAILABILITY

The Hartree Fock code used in this work will be available on GitHub upon publication and the data generated using this code is available through request to the authors.

[1] Z. Tešanović, F. m. c. Axel, and B. I. Halperin, “hall crystal” versus wigner crystal, *Phys. Rev. B* **39**, 8525 (1989).

[2] T. Soejima, J. Dong, A. Vishwanath, and D. E. Parker, λ -Jellium Model for the Anomalous Hall Crystal, *Physical Review Letters* **135**, 186505 (2025), publisher: American Physical Society.

[3] F. Desrochers, J. Huxford, M. R. Hirsbrunner, and Y. B. Kim, *Electronic Crystal Phases in the Presence of Non-Uniform Berry Curvature and Tunable Berry Flux: The λ -Jellium model* (2025), arXiv:2509.15300 [cond-mat].

[4] K.-S. Kim, Magnetic interactions of wigner crystal in magnetic field and berry curvature: Multi-particle tunneling through complex trajectories (2025), arXiv:2508.13149.

[5] S. Joy, L. Levitov, and B. Skinner, *Chiral Wigner crystal phases induced by Berry curvature* (2025), arXiv:2507.22121 [cond-mat].

[6] A. P. Reddy and L. Fu, *Quantum melting a Wigner crystal into Hall liquids* (2025), arXiv:2508.21000 [cond-mat].

[7] Z. Lu, T. Han, Y. Yao, A. P. Reddy, J. Yang, J. Seo, K. Watanabe, T. Taniguchi, L. Fu, and L. Ju, Fractional quantum anomalous Hall effect in multilayer graphene, *Nature* **626**, 759 (2024), publisher: Nature Publishing Group.

[8] Z. Lu, T. Han, Y. Yao, Z. Hadjri, J. Yang, J. Seo, L. Shi, S. Ye, K. Watanabe, T. Taniguchi, and L. Ju, Extended quantum anomalous Hall states in graphene/hBN moiré superlattices, *Nature* **637**, 1090 (2025), publisher: Nature Publishing Group.

[9] J. Xie, Z. Huo, X. Lu, Z. Feng, Z. Zhang, W. Wang, Q. Yang, K. Watanabe, T. Taniguchi, K. Liu, Z. Song, X. C. Xie, J. Liu, and X. Lu, Tunable fractional Chern insulators in rhombohedral graphene superlattices, *Nature Materials* **24**, 1042 (2025), publisher: Nature Publishing Group.

[10] H. Zhang, Q. Li, M. G. Scheer, R. Wang, C. Tuo, N. Zou, W. Chen, J. Li, X. Cai, C. Bao, M.-R. Li, K. Deng, K. Watanabe, T. Taniguchi, M. Ye, P. Tang, Y. Xu, P. Yu, J. Avila, P. Dudin, J. D. Denlinger, H. Yao, B. Lian, W. Duan, and S. Zhou, Correlated topological flat bands in rhombohedral graphite, *Proceedings of the National Academy of Sciences* **121**, e2410714121 (2024), publisher: Proceedings of the National Academy of Sciences.

[11] H. Zhang, J. Lu, K. Liu, Y. Wang, F. Wang, S. Wu, W. Chen, X. Cai, K. Watanabe, T. Taniguchi, J. Avila, P. Dudin, M. D. Watson, A. Louat, T. Sato, P. Yu, W. Duan, Z. Song, G. Chen, and S. Zhou, Moiré enhanced flat band in rhombohedral graphene, *Nature Materials* **1** (2025), publisher: Nature Publishing Group.

[12] S. H. Aronson, T. Han, Z. Lu, Y. Yao, J. P. Butler, K. Watanabe, T. Taniguchi, L. Ju, and R. C. Ashoori, Displacement Field-Controlled Fractional Chern Insulators and Charge Density Waves in a Graphene/hBN Moiré Superlattice, *Physical Review X* **15**, 031026 (2025).

[13] J. Dong, Anomalous Hall Crystals in Rhombohedral Multilayer Graphene. I. Interaction-Driven Chern Bands and Fractional Quantum Hall States at Zero Magnetic Field, *Physical Review Letters* **133**, 10.1103/PhysRevLett.133.206503 (2024).

[14] J. Dong, A. S. Patri, and T. Senthil, Theory of Quantum Anomalous Hall Phases in Pentalayer Rhombohedral Graphene Moiré Structures, *Physical Review Letters* **133**, 206502 (2024), publisher: American Physical Society.

[15] J. Dong, A. S. Patri, and T. Senthil, Stability of anomalous Hall crystals in multilayer rhombohedral graphene, *Physical Review B* **110**, 205130 (2024), publisher: Amer-

ican Physical Society.

[16] B. Zhou, H. Yang, and Y.-H. Zhang, Fractional quantum anomalous hall effect in rhombohedral multilayer graphene in the moiréless limit, *Phys. Rev. Lett.* **133**, 206504 (2024).

[17] B. Zhou and Y.-H. Zhang, New Classes of Quantum Anomalous Hall Crystals in Multilayer Graphene, *Physical Review Letters* **135**, 036501 (2025), publisher: American Physical Society.

[18] T. Tan and T. Devakul, Parent Berry Curvature and the Ideal Anomalous Hall Crystal, *Physical Review X* **14**, 041040 (2024), publisher: American Physical Society.

[19] T. Tan, J. May-Mann, and T. Devakul, Variational Wave-Function Analysis of the Fractional Anomalous Hall Crystal, *Physical Review Letters* **135**, 036604 (2025), publisher: American Physical Society.

[20] Z. Guo and J. Liu, Correlation stabilized anomalous Hall crystal in bilayer graphene (2025), arXiv:2409.14658 [cond-mat].

[21] T. Soejima, J. Dong, T. Wang, T. Wang, M. P. Zale-tel, A. Vishwanath, and D. E. Parker, Anomalous Hall crystals in rhombohedral multilayer graphene. II. General mechanism and a minimal model, *Physical Review B* **110**, 205124 (2024), publisher: American Physical Society.

[22] B. A. Bernevig and Y. H. Kwan, "Berry Trashcan" Model of Interacting Electrons in Rhombohedral Graphene (2025), arXiv:2503.09692 [cond-mat].

[23] T. Tan, P. J. Ledwith, and T. Devakul, The ideal limit of rhombohedral graphene: Interaction-induced layer-skyrmion lattices and their collective excitations (2025), arXiv:2511.07402 [cond-mat].

[24] F. Desrochers, M. R. Hirsbrunner, J. Huxford, A. S. Patri, T. Senthil, and Y. B. Kim, Elastic response and instabilities of anomalous hall crystals (2025), arXiv:2503.08784.

[25] Z. Wei, A.-K. Wu, M. Gonçalves, and S.-Z. Lin, Edge-driven transition between extended quantum anomalous Hall crystal and fractional Chern insulator in rhombohedral graphene multilayers, *Physical Review B* **111**, 035116 (2025), arXiv:2409.05043 [cond-mat].

[26] K. Huang, S. Das Sarma, and X. Li, Fractional quantum anomalous Hall effect in rhombohedral multilayer graphene with a strong displacement field, *Physical Review B* **111**, 075130 (2025), publisher: American Physical Society.

[27] E. Aguilar-Méndez, T. Neupert, and G. Wagner, Full, three-quarter, half and quarter Wigner crystals in Bernal bilayer graphene (2025), arXiv:2505.09685 [cond-mat].

[28] Z. Guo, X. Lu, B. Xie, and J. Liu, Fractional Chern insulator states in multilayer graphene moiré superlattices, *Physical Review B* **110**, 075109 (2024), publisher: American Physical Society.

[29] Y. H. Kwan, J. Yu, J. Herzog-Arbeitman, D. K. Efetov, N. Regnault, and B. A. Bernevig, Moiré fractional Chern insulators. III. Hartree-Fock phase diagram, magic angle regime for Chern insulator states, role of moiré potential, and Goldstone gaps in rhombohedral graphene superlattices, *Physical Review B* **112**, 075109 (2025), publisher: American Physical Society.

[30] M. Uzan, W. Zhi, M. Bocarsly, J. Dong, S. Dutta, N. Auerbach, N. S. Kander, M. Labendik, Y. Myasoe-dov, M. E. Huber, K. Watanabe, T. Taniguchi, D. E. Parker, and E. Zeldov, hbn alignment orientation con-trols moiré strength in rhombohedral graphene (2025), arXiv:2507.20647.

[31] F. Zhang, J. Jung, G. A. Fiete, Q. Niu, and A. H. MacDonald, Spontaneous quantum hall states in chirally stacked few-layer graphene systems, *Phys. Rev. Lett.* **106**, 156801 (2011).

[32] W. Chen and J. L. Lado, Interaction-driven surface chern insulator in nodal line semimetals, *Phys. Rev. Lett.* **122**, 016803 (2019).

[33] A. Lau, T. Hyart, C. Autieri, A. Chen, and D. I. Pikulin, Designing three-dimensional flat bands in nodal-line semimetals, *Phys. Rev. X* **11**, 031017 (2021).

[34] J. Herzog-Arbeitman, Y. Wang, J. Liu, P. M. Tam, Z. Qi, Y. Jia, D. K. Efetov, O. Vafek, N. Regnault, H. Weng, Q. Wu, B. A. Bernevig, and J. Yu, Moiré fractional Chern insulators. II. First-principles calculations and continuum models of rhombohedral graphene superlattices, *Physical Review B* **109**, 205122 (2024), publisher: American Physical Society.

[35] Z. Dong, M. Davydova, O. Ogunnaike, and L. Levitov, Isospin- and momentum-polarized orders in bilayer graphene, *Physical Review B* **107**, 075108 (2023).

[36] H. Zhou, T. Xie, A. Ghazaryan, T. Holder, J. R. Ehrerts, E. M. Spanton, T. Taniguchi, K. Watanabe, E. Berg, M. Serbyn, and A. F. Young, Half- and quarter-metals in rhombohedral trilayer graphene, *Nature* **598**, 429 (2021), publisher: Nature Publishing Group.

[37] J. M. Koh, J. Alicea, and E. Lantagne-Hurtubise, Correlated phases in spin-orbit-coupled rhombohedral trilayer graphene, *Physical Review B* **109**, 035113 (2024).

[38] J. M. Koh, A. Thomson, J. Alicea, and E. Lantagne-Hurtubise, Symmetry-broken metallic orders in spin-orbit-coupled Bernal bilayer graphene, *Physical Review B* **110**, 245118 (2024), arXiv:2407.09612 [cond-mat].

[39] Z. Liu and J. Wang, Layer-dependent quantum anomalous Hall effect in rhombohedral graphene, *Physical Review B* **111**, L081111 (2025).

[40] Y. H. Kwan, Z. Wang, G. Wagner, N. Bultinck, S. H. Simon, and S. A. Parameswaran, Mean-field Modelling of Moiré Materials: A User's Guide with Selected Applications to Twisted Bilayer Graphene (2025), arXiv:2511.21683 [cond-mat].

[41] X. Lu, B. Xie, and J. Liu, A numerical perspective on moiré superlattices: From single-particle properties to many-body physics (2025), arXiv:2512.07115.

[42] C.-H. Huang, C. Huang, and M. A. Cazalilla, Competition of exchange and correlation energies in two-dimensional N -component electron gas ferromagnetism, *Physical Review B* **111**, 045129 (2025).

[43] A. Herasymchuk, S. G. Sharapov, O. V. Yazyev, and Y. Zhumagulov, Correlated phases in rhombohedral N-layer graphene (2025), arXiv:2508.14630 [cond-mat].

[44] G. Parra-Martínez, A. Jimeno-Pozo, J. A. Silva-Guillén, and F. Guinea, Nematic and partially polarized phases in rhombohedral graphene with varying number of layers: An extensive Hartree-Fock study, *Adv. Mater.* , e14008 (2025).

[45] K. Kudo, R. Nakai, and K. Nomura, Quantum anomalous, spin, and valley hall effects in pentalayer rhombohedral graphene moiré superlattices, *Phys. Rev. B* **110**, 245135 (2024).

[46] T. Uchida, T. Kawakami, and M. Koshino, Non-Abelian Chern band in rhombohedral graphene multilayers (2025), arXiv:2508.07366 [cond-mat].

[47] S. Chatterjee, T. Wang, E. Berg, and M. P. Zaletel, Inter-valley coherent order and isospin fluctuation mediated superconductivity in rhombohedral trilayer graphene, *Nature Communications* **13**, 6013 (2022).

[48] N. Auerbach, S. Dutta, M. Uzan, Y. Vituri, Y. Zhou, A. Y. Meltzer, S. Grover, T. Holder, P. Emanuel, M. E. Huber, Y. Myasoedov, K. Watanabe, T. Taniguchi, Y. Oreg, E. Berg, and E. Zeldov, Isospin magnetic texture and intervalley exchange interaction in rhombohedral tetralayer graphene, *Nature Physics* **21**, 1765–1772 (2025).

[49] S. Joy and B. Skinner, Disorder-induced liquid-solid phase coexistence in 2D electron systems (2025), arXiv:2502.11235 [cond-mat].

[50] S. Das Sarma and M. Xie, Thermal crossover from a chern insulator to a fractional chern insulator in pentalayer graphene, *Phys. Rev. B* **110**, 155148 (2024).

[51] J. Dong, O. E. Sommer, T. Soejima, D. E. Parker, and A. Vishwanath, Phonons in electron crystals with Berry curvature, *Proceedings of the National Academy of Sciences* **122**, e2515532122 (2025), publisher: Proceedings of the National Academy of Sciences.

[52] H. C. Po, H. Watanabe, and A. Vishwanath, Fragile topology and wannier obstructions, *Phys. Rev. Lett.* **121**, 126402 (2018).

[53] A. S. Patri, Z. Dong, and T. Senthil, Extended quantum anomalous Hall effect in moiré structures: Phase transitions and transport, *Physical Review B* **110**, 245115 (2024), publisher: American Physical Society.

[54] Y. Zeng and A. J. Millis, Berry Phase Dynamics of Sliding Electron Crystals, *Physical Review X* **15**, 031059 (2025), publisher: American Physical Society.

[55] Y. Shao and X. Dai, Electrical breakdown of excitonic insulators, *Phys. Rev. X* **14**, 021047 (2024).

[56] Y. Wang, J. An, C. Ye, X. Wang, D. Mai, H. Zhao, Y. Zhang, C. Peng, K. Watanabe, T. Taniguchi, X. Sun, R. Dai, Z. Wang, W. Qin, Z. Qiao, and Z. Zhang, Pressure-driven moiré potential enhancement and tertiary gap opening in graphene/h-bn heterostructure, *Phys. Rev. Lett.* **135**, 046303 (2025).

[57] N. Morales-Durán, J. Wang, G. R. Schleider, M. Angeli, Z. Zhu, E. Kaxiras, C. Repellin, and J. Cano, Pressure-enhanced fractional Chern insulators along a magic line in moiré transition metal dichalcogenides, *Physical Review Research* **5**, L032022 (2023), publisher: American Physical Society.

[58] B. Wang, J. Yu, P. Sharma, and C.-C. Liu, Pressure-tunable generalized wigner crystal and fractional chern insulator in twisted mote₂ (2025), arXiv:2504.11177.

[59] S. A. A. Ghorashi, A. Dunbrack, A. Abouelkomsan, J. Sun, X. Du, and J. Cano, Topological and stacked flat bands in bilayer graphene with a superlattice potential, *Phys. Rev. Lett.* **130**, 196201 (2023).

[60] W. Miao, A. Rashidi, and X. Dai, Artificial moiré engineering for an ideal bernevig-hughes-zhang model, *Phys. Rev. B* **111**, 045113 (2025).

[61] Y. Shi, B. Xie, F. Ren, X. Cai, Z. Guo, Q. Li, X. Lu, N. Regnault, Z. Liu, and J. Liu, Fractional topological states in rhombohedral multilayer graphene modulated by kagome superlattice (2025), arXiv:2502.17320.

[62] Z. Huo, W. Wang, J. Xie, Y. H. Kwan, J. Herzog-Arbeitman, Z. Zhang, Q. Yang, M. Wu, K. Watanabe, T. Taniguchi, K. Liu, N. Regnault, B. A. Bernevig, and X. Lu, Does moiré matter? critical moiré dependence with quantum fluctuations in graphene based integer and fractional chern insulators (2025), arXiv:2510.15309.

[63] A. Valenti, Y. Vituri, Y. Yang, D. E. Parker, T. Soejima, J. Dong, M. A. Morales, A. Vishwanath, E. Berg, and S. Zhang, Quantum geometry driven crystallization: A neural-network variational monte carlo study (2025), arXiv:2512.07947.

[64] X. Lu, Y. Yang, Z. Guo, and J. Liu, General Many-Body Perturbation Framework for Moiré Systems (2025), arXiv:2509.19764 [cond-mat].

[65] J. P. Eisenstein, L. N. Pfeiffer, and K. W. West, Negative compressibility of interacting two-dimensional electron and quasiparticle gases, *Phys. Rev. Lett.* **68**, 674 (1992).

[66] J. P. Eisenstein, L. N. Pfeiffer, and K. W. West, Compressibility of the two-dimensional electron gas: Measurements of the zero-field exchange energy and fractional quantum hall gap, *Phys. Rev. B* **50**, 1760 (1994).

[67] B. Spivak and S. A. Kivelson, Phases intermediate between a two-dimensional electron liquid and wigner crystal, *Phys. Rev. B* **70**, 155114 (2004).

[68] G. Rai, L. Crippa, D. Călugăru, H. Hu, F. Paoletti, L. de' Medici, A. Georges, B. A. Bernevig, R. Valentí, G. Sangiovanni, and T. Wehling, Dynamical correlations and order in magic-angle twisted bilayer graphene, *Phys. Rev. X* **14**, 031045 (2024).

[69] A. Datta, M. J. Calderón, A. Camjayi, and E. Bascones, Heavy quasiparticles and cascades without symmetry breaking in twisted bilayer graphene, *Nat. Commun.* **14**, 5036 (2023).

[70] T. Han, Z. Lu, Z. Hadjri, L. Shi, Z. Wu, W. Xu, Y. Yao, A. A. Cotten, O. Sharifi Sedeh, H. Weldeyesus, J. Yang, J. Seo, S. Ye, M. Zhou, H. Liu, G. Shi, Z. Hua, K. Watanabe, T. Taniguchi, P. Xiong, D. M. Zumbühl, L. Fu, and L. Ju, Signatures of chiral superconductivity in rhombohedral graphene, *Nature* **643**, 654 (2025), publisher: Nature Publishing Group.

[71] R. Q. Nguyen, H.-T. Wu, E. Morissette, N. J. Zhang, P. Qin, K. Watanabe, T. Taniguchi, A. W. Hui, D. E. Feldman, and J. I. A. Li, A hierarchy of superconductivity and topological charge density wave states in rhombohedral graphene (2025), arXiv:2507.22026.

[72] G. Kresse and J. Furthmüller, Efficient iterative schemes for ab initio total-energy calculations using a plane-wave basis set, *Phys. Rev. B* **54**, 11169 (1996).

[73] J. P. Perdew, K. Burke, and M. Ernzerhof, Generalized gradient approximation made simple, *Phys. Rev. Lett.* **77**, 3865 (1996).

[74] P. E. Blöchl, Projector augmented-wave method, *Phys. Rev. B* **50**, 17953 (1994).

[75] S. Grimme, J. Antony, S. Ehrlich, and H. Krieg, A consistent and accurate ab initio parametrization of density functional dispersion correction (DFT-D) for the 94 elements H-Pu, *J. Chem. Phys.* **132**, 154104 (2010).

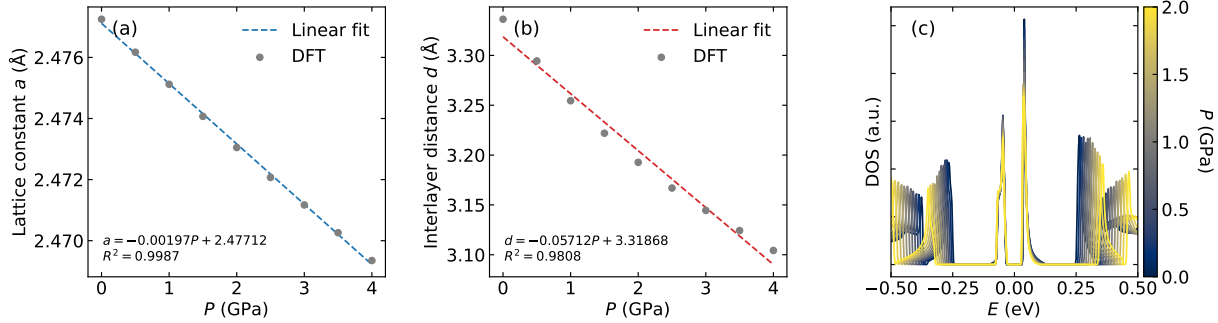


FIG. 6. (a) (b) The relaxed lattice constant and interlayer distance of R5G under moderate pressure. The grey dots are extracted from DFT calculations and the linear fit is in use for calculate the phase diagram in Fig. 5. (c) Calculated density of state for R5G under pressure.

Appendix A: DFT under pressure

To determine the interlayer spacing and lattice constant of graphene under pressure, we performed density functional theory (DFT) calculations using the Vienna Ab initio Simulation Package (VASP) [72]. The exchange–correlation effects were treated within the generalized gradient approximation using the revised Perdew–Burke–Ernzerhof (RPBE) functional [73], together with projector augmented-wave (PAW) pseudopotentials [74]. Van der Waals interactions were included via the DFT-D3 correction scheme [75]. Pentalayer graphene was modeled using a five-layer 3×3 supercell with ABC stacking. Prior to extracting the interlayer distances, all carbon atomic positions were fully relaxed under the applied external pressure. A plane-wave energy cutoff of 520 eV was used for all pressure-dependent calculations. The total energy and force convergence thresholds were set to 10^{-8} eV and 10^{-3} eV \AA^{-1} , respectively. The relaxed lattice constant a and interlayer distance d is shown in Fig. 6.

Appendix B: Hartree Fock

To perform the Hartree Fock calculations, we first project the interacting Hamiltonian Eq. 4 onto active subspace,

$$H_{\text{int}} = \frac{1}{2N_{\bar{\mathbf{k}}}} \sum_{\bar{\mathbf{k}}, \bar{\mathbf{k}'}, \bar{\mathbf{q}}} \sum_{\mu\mu'} \sum_{ss'} \sum_{nmn'm'} \left(\sum_{\mathbf{Q}} v(\mathbf{Q} + \bar{\mathbf{q}}) \lambda_{nm, n'm'}^{\mu\mu'}(\bar{\mathbf{k}}, \bar{\mathbf{k}'}, \bar{\mathbf{q}}, \mathbf{Q}) \right) d_{s\mu n}^\dagger(\bar{\mathbf{k}} + \bar{\mathbf{q}}) d_{s'\mu' n'}^\dagger(\bar{\mathbf{k}'}) d_{s'\mu' m'}(\bar{\mathbf{k}'}) d_{s\mu m}(\bar{\mathbf{k}}), \quad (\text{B1})$$

where $\bar{\mathbf{k}}, \bar{\mathbf{k}'}, \bar{\mathbf{q}}$ are momentums defined in the mini Brillouin zone (mBZ) due to band folding, $N_{\bar{\mathbf{k}}}$ is the number of momentum points in the mBZ grid. \mathbf{G}, \mathbf{Q} are reciprocal lattice vectors. The form factor is defined as

$$\lambda_{nm, n'm'}^{\mu\mu' ss'}(\bar{\mathbf{k}}, \bar{\mathbf{k}'}, \bar{\mathbf{q}}, \mathbf{Q}) = \sum_{\alpha\alpha' \mathbf{G}\mathbf{G}'} C_{\mu\alpha s\mathbf{G}+\mathbf{Q}, n}^*(\bar{\mathbf{k}} + \bar{\mathbf{q}}) C_{\mu'\alpha' s' \mathbf{G}'-\mathbf{Q}, n'}^*(\bar{\mathbf{k}'}) C_{\mu'\alpha' s' \mathbf{G}', m'}(\bar{\mathbf{k}'}) C_{\mu\alpha s\mathbf{G}, m}(\bar{\mathbf{k}}). \quad (\text{B2})$$

where we take advantage of

$$d_{s\mu n}(\bar{\mathbf{k}}) = \sum_{\alpha\mathbf{G}} C_{\mu\alpha s\mathbf{G}, n}(\bar{\mathbf{k}}) c_{\mu\alpha s}(\bar{\mathbf{k}} + \mathbf{G}). \quad (\text{B3})$$

We now formulate the band-projected Hartree Fock theory in the Green's-function framework, where the mean field corrections naturally appear as static self energy correction in the Dyson equation. In the mBZ, we use composite band indices $\eta = (s, \mu, n)$, where s denotes spin, μ the valley, and n the band index. The single particle Green's function is defined as $[G(\bar{\mathbf{k}}, \tau)]_{\eta\eta'} = -\langle T_\tau c_{\bar{\mathbf{k}}, \eta}(\tau) c_{\bar{\mathbf{k}}, \eta'}^\dagger(0) \rangle$, satisfying the Dyson equation $G^{-1}(\bar{\mathbf{k}}, i\omega_n) = i\omega_n + \mu - H_0(\bar{\mathbf{k}}) - \Sigma(\bar{\mathbf{k}}, i\omega_n)$, where $H_0(\bar{\mathbf{k}})$ is the single particle Hamiltonian projected to the chosen band subspace. In the HF approximation, the self-energy is static, $\Sigma(\bar{\mathbf{k}}, i\omega_n) \equiv \Sigma(\bar{\mathbf{k}})$. The single particle density matrix is defined as $\rho_{\eta\eta'}(\bar{\mathbf{k}}) = \langle c_{\bar{\mathbf{k}}, \eta}^\dagger c_{\bar{\mathbf{k}}, \eta'} \rangle$, and the total self energy consists of Hartree and Fock components, $\Sigma = \Sigma^H + \Sigma^F$. These are expressed through four-index form factors Λ constructed from the Bloch coefficients of the projected bands. The Hartree and Fock contributions

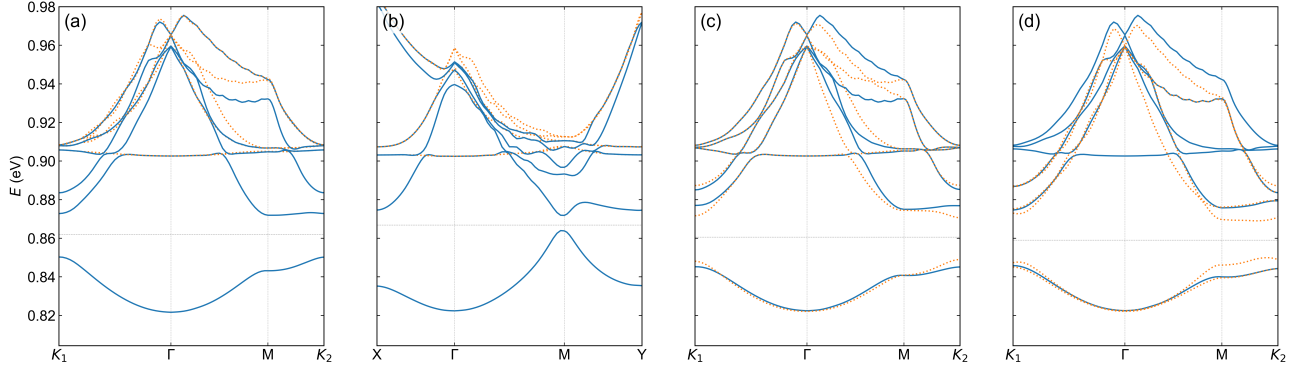


FIG. 7. Hartree Fock band structures for representative anomalous Hall crystal (AHC) states. Blue solid lines denote spin-down bands and orange dashed lines denote spin-up bands. (a) AHC ($C = 1$) on a hexagonal lattice at $n = 1 \times 10^{12} \text{ cm}^{-2}$; one occupied (or low-energy) band is topological while the other is topologically trivial. (b) AHC ($C = 1$) on a square lattice at $n = 1 \times 10^{12} \text{ cm}^{-2}$; one band is topological and the other is trivial. (c) AHC ($C = 1$) on a hexagonal lattice at $n = 2 \times 10^{12} \text{ cm}^{-2}$; one band is topological and the other is trivial. (d) AHC ($C = 1$) on a hexagonal lattice at $n = 3 \times 10^{12} \text{ cm}^{-2}$; one band is topological and two bands are trivial.

are given by

$$[\Sigma^H(\bar{\mathbf{k}})]_{\eta\eta'} = \frac{1}{N_{\bar{\mathbf{k}}}} \sum_{\bar{\mathbf{k}}', \zeta, \zeta', \mathbf{Q}} v(\mathbf{Q}) \Lambda_{\eta\eta'; \zeta\zeta'}^H(\bar{\mathbf{k}}, \bar{\mathbf{k}}'; \mathbf{Q}) \rho_{\zeta'\zeta}(\bar{\mathbf{k}}'), \quad (\text{B4})$$

$$[\Sigma^F(\bar{\mathbf{k}})]_{\eta\eta'} = -\frac{1}{N_{\bar{\mathbf{k}}}} \sum_{\bar{\mathbf{k}}', \zeta, \zeta', \mathbf{Q}} v(\bar{\mathbf{k}}' - \bar{\mathbf{k}} + \mathbf{Q}) \Lambda_{\eta\zeta; \zeta'\eta'}^F(\bar{\mathbf{k}}, \bar{\mathbf{k}}'; \mathbf{Q}) \rho_{\zeta'\zeta}(\bar{\mathbf{k}}'), \quad (\text{B5})$$

where $N_{\bar{\mathbf{k}}}$ is the number of momentum points in the mBZ grid. The tensors $\Lambda^{H/F}$ entering the self-energies are directly related to the four-index projected form factors λ : $\Lambda_{\eta\eta'; \zeta\zeta'}^H(\bar{\mathbf{k}}, \bar{\mathbf{k}}'; \mathbf{Q}) = \lambda_{nm, n'm'}^{\mu\mu'}(\bar{\mathbf{k}}, \bar{\mathbf{k}}', \bar{\mathbf{q}} = 0, \mathbf{Q})$ for the Hartree channel, and $\Lambda_{\eta\zeta; \zeta'\eta'}^F(\bar{\mathbf{k}}, \bar{\mathbf{k}}'; \mathbf{Q}) = \lambda_{nm, n'm'}^{\mu\mu'}(\bar{\mathbf{k}}, \bar{\mathbf{k}}', \bar{\mathbf{q}} = \bar{\mathbf{k}}' - \bar{\mathbf{k}}, \mathbf{Q})$ for the Fock channel, with composite indices $\eta = (s, \mu, n)$, $\eta' = (s, \mu, m)$, $\zeta = (s', \mu', m')$, and $\zeta' = (s', \mu', n')$. The self-consistent HF equations are then solved in the Dyson framework: starting from an initial random single particle density matrix across different spin-valley flavors. The Hartree and Fock self-energies are evaluated via the above four-index contractions, forming the static Dyson Hamiltonian $H_{\text{HF}} = H_0 + \Sigma^H + \Sigma^F$, the Dyson equation is solved to obtain an updated Green's function and density matrix, and the process is iterated with mixing until both the density matrix and self-energy converge. At convergence, $\Sigma(\bar{\mathbf{k}})$ defines the quasiparticle spectrum of RMG electrons. The total energy is calculated through,

$$E = \sum_{\bar{\mathbf{k}}} \text{Tr} \left((H(\bar{\mathbf{k}}) + \frac{1}{2} \Sigma(\bar{\mathbf{k}})) \rho(\bar{\mathbf{k}}) \right). \quad (\text{B6})$$

The real space density $\rho(\mathbf{r})$ can also be obtained,

$$\rho(\mathbf{r}) = \sum_{\mathbf{G}} \rho(\mathbf{G}) e^{i\mathbf{G} \cdot \mathbf{r}}, \quad \rho(\mathbf{G}) = \frac{1}{N_{\mathbf{k}}^2} \sum_{\bar{\mathbf{k}}mn} \langle u_m^{\text{HF}}(\bar{\mathbf{k}}) | u_n^{\text{HF}}(\bar{\mathbf{k}} + \mathbf{G}) \rangle \quad (\text{B7})$$

where $|u_n^{\text{HF}}\rangle$ is the wavefunction of the n -th converged occupied Hartree-Fock band. In all calculations throughout this paper, we only preserve 3 conduction bands, 4 shells of plane waves and freeze all valence bands of RMG due to the relatively large displacement field we concern. Typical Hartree Fock quasi-particle band structures for these electronic phases are shown in Fig. 7 with different doping densities and real space geometry.

Appendix C: Finite size scaling

To minimize finite size effects and enable a controlled comparison of mean-field condensation energies among electronic crystal states with different lattice geometries, we perform self-consistent HF calculations on a sequence

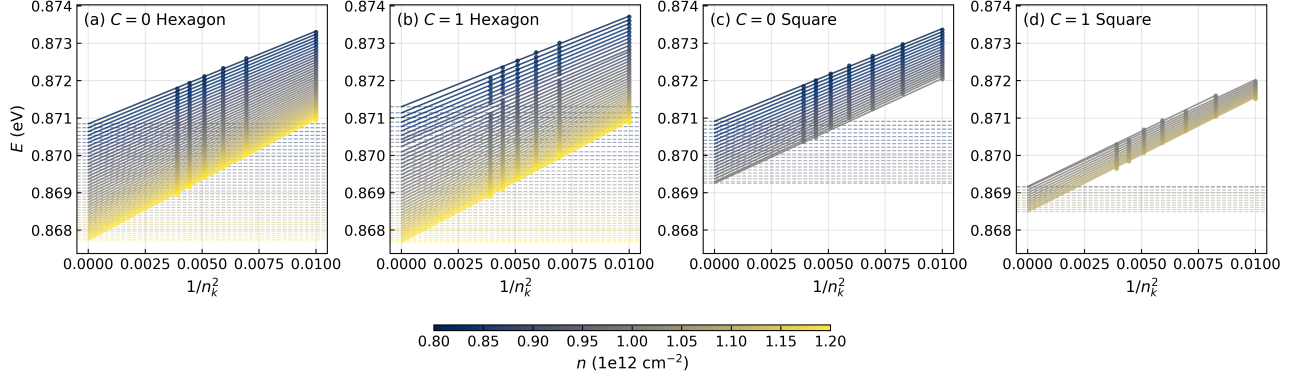


FIG. 8. Finite size scaling of the HF condensation energy for electronic crystal states with different lattice geometries. The condensation energy per particle, $E(n_k)$, is computed on (n_k, n_k) k -meshes and linearly extrapolated in $1/n_k^2$ to the $n_k \rightarrow \infty$ limit. The intercept $E(n_k \rightarrow \infty)$ is used to produce Fig. 4 in the main text.

of increasingly dense (n_k, n_k) momentum meshes. For each mesh we evaluate the condensation energy per particle, $E(n_k)$. Since the dominant discretization error is expected to scale with the inverse number of sampled k points, $N_k = n_k^2$, we extrapolate to the thermodynamic limit by fitting $E(n_k)$ linearly in $1/n_k^2$, $E(n_k) = E(n_k \rightarrow \infty) + \frac{a}{n_k^2}$. The intercept $E(n_k \rightarrow \infty)$ is taken as the infinite k -mesh estimate, and the same extrapolation protocol is applied to all candidate geometries to ensure an unbiased energy comparison. The results is shown in Fig. 8.